Exploring the role of electronic structure on photo-catalytic behavior of carbon-nitride polymorphs

Sujoy Datta

Department of Physics, University of Calcutta, Kolkata 700009, India

Department of Physics, Lady Brabourne College, Kolkata 700017, India

Prashant Singh[1]

Ames Laboratory, U.S. Department of Energy, Iowa State University, Ames, Iowa 50011, USA

Debnarayan Jana

Department of Physics, University of Calcutta, Kolkata 700009, India

Chhanda B Chaudhuri

Department of Physics, Lady Brabourne College, Kolkata 700017, India

Manoj K Harbola

Department of Physics, Indian Institute of Technology, Kanpur, 208016, India

Duane D. Johnson[1]

Ames Laboratory, U.S. Department of Energy, Iowa State University, Ames, Iowa 50011, USA

Materials Science & Engineering, Iowa State University, Ames, Iowa 50011, USA

Abhijit Mookerjee

S. N. Bose National Centre for Basic Sciences, Salt Lake City, Kolkata 700098, India

Abstract

A fully self-consistent density-functional theory (DFT) with improved functionals is used to provide a comprehensive account of structural, electronic, and optical properties of C_3N_4 polymorphs. Using our recently developed van Leeuwen-Baerends (vLB) corrected local-density approximation (LDA), we implemented LDA+vLB within full-potential N^{th}-order muffin-tin orbital (FP-NMTO) method and show that it improves structural properties and band gaps compared to semi-local functionals (LDA/GGA). We demonstrate that the LDA+vLB predicts band-structure and work-function for well-studied 2D-graphene and bulk-Si in very good agreement with experiments, and more exact hybrid functional (HSE) calculations as implemented in the Quantum-Espresso (QE) package. The structural and electronic-structure (band gap) properties of C_3N_4 polymorphs calculated using FP-NMTO-LDA+vLB is compared with more sophisticated hybrid-functional calculations. We also perform detailed investigation of photocatalytic behavior using QE-HSE method of C_3N_4 polymorphs through work-function, band (valence and conduction) position with respect to water reduction and oxidation potential. Our results show γ-C_3N_4 as the best candidate for photocatalysis among all the C_3N_4 polymorphs but it is dynamically unstable at 'zero' pressure. We show that γ-C_3N_4 can be stabilized under hydrostatic-pressure, which improves its photocatalytic behavior relative to water reduction and oxidation potentials.

Keywords: Density-functional theory, graphene, semiconductor, band gap, photocatalysis

1. Introduction

Conjugated carbon-nitride (C_3N_4) polymers have drawn broad interdisciplinary attention as metal-free and visible-light-responsive photo-catalysts for solar-energy conversion and environmental remediation [1–3], especially for their appealing electronic dispersion, high physicochemical stabilities, and earth-abundant elements. Though experimental works on graphitic carbon nitrides, both on triazine (t-g) and heptazine (h-g) structures, are prolific, the low specific surface area and high defect density remains a concern on its photocatalytic performance. Among other experimental techniques, combination of graphitic-$C_3N_4$with three dimensional hydrogel framework, exfoliation into nanosheets, construction of graphitic-C_3N_4 based heterojunction systems are widely investigated [4, 5]. Beside experimental trials, a plethora of first principles calculations are also aimed to improve the photocatalytic activity of graphitic-C_3N_4 and its derivatives [6, 7]. Notably, doping (e.g., by S or Si) or hybridization with other photocatalyst enhances the photo-reactive performance of graphitic-C_3N_4 [8, 9]. The large band gap tunability makes C_3N_4 derivatives potential candidates for CO_2 capture, control of pollutants [10], water splitting, or energy-storage devices [10, 11].

Carbon-nitride is found in amorphous and various crystalline forms [12, 13], with distinctly different characteristics (similar to two crystalline forms of carbon: graphite and diamond). However, first-principles electronic-structure and optical properties of the known C_3N_4 polymorphs are sparse. Using density-functional theory (DFT) methods, we investigate the structural, electronic, and optical properties of C_3N_4 polymorphs, specifically: (i) α, (ii) β, (iii) *cubic*, (iv) γ (spinel), (v) $t-g$(AA) [AA-stacked graphitic-triazine], (vi) $t-g$(AB) [AB-stacked graphitic-triazine], and (vii) $h-g$ [AA-stacked graphitic-heptazine].

The LDA or GGA exchange-correlation (XC) functionals [14, 15] are known to provide a reasonable account of structural properties, but show limitations and often miserably fail in predicting band gaps [16–18]. To address C_3N_4 polymorphs, we use our recently developed van Leeuwen-Baerends (vLB) corrected LDA (LDA+vLB) exchange [19] implemented both in tight-binding linearized muffin-tin orbital (TB-LMTO) [20, 21] and in full-potential N^{th}-order muffin-tin orbital (FP-NMTO) [22]. The LDA+vLB is similar to a modified-LDA [23] and mimics the orbital-dependent, exact-exchange potentials [24] and notably requires a computational cost similar to the semi-local XC, like LDA or GGA. Notably, the advantage of our approach lies in the fact that the LDA+vLB greatly improves the band gap relative to traditional (semi)local functionals, with speed of semi-local functionals and accuracy of advanced hybrid-functional (e.g. HSE) or GW functionals [19, 24–28]. Our LDA+vLB calculated band-structure of 2-dimensional (2D) graphene and bulk-Si show good agreement to experiments [29] (see supplement), and with hybrid-functionals (HSE) [30] as implemented in the Quantum-Espresso (QE) package [31, 32]).

Considering the fact that most semi-local functionals underestimate band-energies and band gap [16, 18], we employ self-consistent QE-HSE to calculate optical properties, work functions, and photocatalytic behavior of C_3N_4 polymorphs. We calculate work-functions of well-studied 2D-graphene [33] and bulk-Si [34] to showcase agreement between prediction and experiments. Our study of C_3N_4 polymorphs finds better optical and photocatalytic behavior of γ-C_3N_4 compared to other polymorphs. However, we find γ-phase exhibits a dynamical instability, i.e., unstable phonon modes with imaginary frequencies. Therefore, we theoretically assess the structural stability versus pressure to find the dynamical stability of γ-phase, and then fully detail the unstable and stable phonon dispersion. Under pressure, the dynamically stable γ-C_3N_4 also satisfies the Born structural stability criteria for the elastic constants of the structure. Our notable finding is that the dynamically stable γ-C_3N_4 (under applied hydrostatic pressure) also shows much improved photocatalytic behavior.

In this systematic study, we established the robustness of our methodology and then we explored the relevant properties of C_3N_4 polymorphs such as band gap, optical properties, and photocatalytic behavior. Our study reveals the possibility of γ phase as better photocalytic material than graphitic phases, which are traditionally found to be a suitable photo-catalytic material. Beside this, the scheme can further be applied to the appropriate derivatives of C_3N_4 polymorphs and other emergent semiconducting materials.

2. Computational Method

FP-NMTO electronic-structure: Choice of a minimal basis set is always tricky, but tight-binding and FP-NMTO [22] methods provide that platform. The FP-NMTO handles the orbital (l-dependent) and m-dependent downfoldings independently, which is very useful for sp^2-hybridized systems, where p_z orbitals

[1]Corresponding author: Tel: +1-515-294-2457/2122.
Email: psingh84@ameslab.gov, ddj@ameslab.gov

behaves differently than p_x and p_y [22, 35]. As most semi-local functionals fail to estimate the correct band gap of semiconducting materials, we predict band gaps of C_3N_4 polymoprhs using an *in-house* developed LDA+vLB exchange with von-Barth-Hedin correlation for solids [19, 25], as implemented in FP-NMTO [22]. The LDA+vLB potential for given atomic densities (ρ) can be written as

$$v_{xc}(\mathbf{r}) = [v_x^{LDA}(\mathbf{r}) + v_x^{vLB}(\mathbf{r})] + v_c^{LDA}(\mathbf{r}), \quad (1)$$

$$\text{with } v_x^{vLB}(\mathbf{r}) = -\beta\rho^{1/3}(\mathbf{r})\frac{z^2}{1+3\beta\, z\sinh^{-1}(z)} \quad (2)$$

Here, $z = |\nabla\rho(\mathbf{r})|/\rho^{4/3}(\mathbf{r})$ and $\beta = 0.05$.

The LDA+vLB (here onwards we use LDA+vLB instead of FP-NMTO-LDA+vLB) provides improvement to the exchange-potential [27] and better band gaps than other semi-local functionals as gradient correction naturally provides the self-interaction correction (SIC) to the LDA without need of SIC-LDA [36]. Most semi-local functionals fail due to the wrong asymptotic behavior at r$\rightarrow$ 0 and r$\rightarrow\infty$ limits, whereas LDA+vLB produces asymptotically-correct, Coulomb-like ($-1/r$) behavior [19, 37].

The LDA+vLB energies are self-consistently converged to 10^{-6} Ry/atom. We use Anderson method [38] to mix charge densities. For k-space integration via the tetrahedron method, we use k-mesh of ($6\times6\times6$) for α; ($6\times6\times10$) for β; ($4\times4\times4$) for both cubic and spinel (γ); ($6\times6\times8$) for t-g (AA); and ($6\times6\times4$) for t-g(AB) phases.

QE-HSE Optical & Work-Function Properties: We performed band-structure calculations of C_3N_4 polymorphs using HSE as implemented in the QE plane-wave basis [31, 32] and compare that with our LDA+vLB predictions (also see supplement). The LDA+vLB predicted band gaps show very good agreement (see Results) with hybrid-functional and experiments. In addition, the self-consistent QE-HSE is used to calculate the complex dielectric tensor $\epsilon_{\alpha\beta}(\omega)$ within the random phase approximation to analyze the work function and photocatalytic behavior of C_3N_4 polymorphs [31, 32]. For details see supplement (Table S1).

The dielectric tensor $\epsilon_{\alpha\beta}(\omega)$ can be defined as:

$$\epsilon_{\alpha\beta}(\omega) = 1 + \frac{4\pi e^2}{\Omega N_{\mathbf{k}} m^2}\sum_{n,n'}\sum_{\mathbf{k}}\frac{\langle u_{\mathbf{k},n'}|\hat{\mathbf{p}}_\alpha|u_{\mathbf{k},n}\rangle\langle u_{\mathbf{k},n}|\hat{\mathbf{p}}_\beta^\dagger|u_{\mathbf{k},n'}\rangle}{(E_{\mathbf{k},n'}-E_{\mathbf{k},n})^2}$$
$$\left[\frac{f(E_{\mathbf{k},n})}{E_{\mathbf{k},n'}-E_{\mathbf{k},n}+\hbar\omega+i\hbar\Gamma}+\frac{f(E_{\mathbf{k},n})}{E_{\mathbf{k},n'}-E_{\mathbf{k},n}-\hbar\omega-i\hbar\Gamma}\right], \quad (3)$$

where Γ is an adiabatic (inter-broadening) parameter tending to zero. To retain a finite lifetime of all excited-states, we have introduced small positive value of Γ to produce an intrinsic broadening to all exited states. The imaginary part of $\epsilon^i_{\alpha\beta}$ is found first and real part $\epsilon^r_{\alpha\beta}$ is calculated using Kramers-Kronig relation.

$$\epsilon^r_{\alpha\beta}(\omega) = 1 + \frac{2}{\pi}\int_0^\infty \frac{\omega'\epsilon^i_{\alpha\beta}(\omega')}{\omega'^2-\omega^2}d\omega'$$

. Real and imaginary parts of the dielectric function are used to calculate optical conductivity, refractive index and absorption coefficient.[39]

$$\text{Dielectric tensor:} \quad \epsilon_{\alpha\beta} = \epsilon^r_{\alpha\beta} + i\epsilon^i_{\alpha\beta} \quad (4)$$

$$\text{Optical Conductivity: } Re[\sigma_{\alpha\beta}(\omega)] = \frac{\omega}{4\pi}\epsilon^i_{\alpha\beta}(\omega) \quad (5)$$

$$\text{Refractive Index:} \quad \mu_{\alpha\alpha} = n_{\alpha\alpha} + ik_{\alpha\alpha} \quad (6)$$

$$n_{\alpha\alpha}(\omega) = \sqrt{\frac{|\epsilon_{\alpha\alpha}|+\epsilon^r_{\alpha\alpha}}{2}};\ \ k_{\alpha\alpha}(\omega) = \sqrt{\frac{|\epsilon_{\alpha\alpha}|-\epsilon^r_{\alpha\alpha}}{2}}$$

$$\text{Absorption Coefficient: } A_{\alpha\alpha}(\omega) = \frac{2\omega k_{\alpha\alpha}(\omega)}{c} \quad (7)$$

Work-function calculation: For photocatalytic activity, the valence-band maximum (VBM) and conduction-band minimum (CBM) position are equally important as band gaps. Therefore, the accurate calculation of work-function (Φ) becomes important, which is defined as the energy required to remove an electron from a slab surface. The Φ is calculated by taking the difference of vacuum energy (E_{vac}) with respect to Fermi-energy (E_F), i.e., $\Phi = V_{vac} - E_F$ [40]. For semi-infinite surfaces (with sufficient number of layers that reproduces bulk behavior), Φ is the difference of vacuum energy for slab and the Fermi energy of the bulk ($\Phi = V_{vac} - E_F^{Bulk}$). This needs two different calculations, (a) bulk, and (b) slabs (semi-infinite surface). The electrostatic potential within the interstitial region in (a) and (b) works as a common parameter, which should be same for (a) bulk and (b) slab in order to compare the energy levels. The matching bulk and slab values standardizes the energy levels. Also, the presence of microscopic fluctuations of electrostatic potentials in the interstitial region require macroscopic averaging of average planar potential with a window size equal to the inter-slab separation. The average planar potential is the average over the plane parallel to the surface-plane and the direction of microscopic averaging (of planar potential) is perpendicular to that plane [41, 42]. Here, the difference of the macroscopic averages for bulk and slab ($\Delta_V = V^{bulk} - V^{slab}$) works as a constant correctional shift to E_F^{Bulk} that brings equivalence of energy levels of these two separate self-consistent calculations. Finally, Φ can be evaluated as $\Phi = V_{vac} - E_F^{bulk} + (V^{bulk} - V^{slab})$. This is how, we

can get rid of the quantum-size effect in designing slabs for work-function calculation [43]. Furthermore, for the semi-infinite systems, the band gap is not much dependent on the surface, and for intrinsic semiconductors the E_F^{bulk} lies at the mid-point of VBM and CBM; therefore, the exact position of energy bands with respect to vacuum energy can be identified. Each slab is created with four layers and inter-slab vacuum is of 15 Å. We have provided validation test of our approach on 2D-graphene,[33] and bulk-Si [34].

Phonons for dynamical stability: To check the dynamical stability in terms of phonons for γ-C_3N_4, we use first-principles density-functional-perturbation theory (DFPT). The DFPT is a straightforward approach that permits phonons to be calculated by perturbing atomic positions on $2 \times 2 \times 2$ supercell (112 atom/cell) of the original 14 atom/cell. All the atomic coordinates are relaxed up to 10^{-6}eV/Å. The atoms are displaced by 0.01 Å from their equilibrium positions to calculate force constants. We use these force constants to calculate phonon dispersion along the high-symmetry direction of the Brillouin zone of γ-phase [44].

3. Results and Discussion

We discuss band-structure of 2D graphene [45], and bulk-Si [29] calculated using FP-NMTO-LDA+vLB to showcase the applicability of our approach and compared with other theory and experiments. We then study allotropes of C_3N_4, both non-graphitic and graphitic phases, for structural and electronic properties.

Graphene: With a 2D hexagonal structure, graphene is very well-studied form of carbon and considered as the building block of many carbon allotropes [46, 47]. The calculated band-structure (Fig. 1, left-panel) shows zero band gap at the K-point with Dirac (Fermionic) linear dispersion. Here, the zero band gap is attributed to the sub-lattice symmetry of the 2D graphene.

Bulk Si: The predicted band gap of bulk-Si (1.25 eV) using LDA+vLB (Fig. 1, right-panel) is also in good agreement with hybrid-functional (1.24 eV) and experiments (1.17 eV) [29]. Notably, we reproduce the indirect ($\Gamma - X$) nature of Si band gap [25], which is not found by standard semi-local XC, for example LDA/GGA [14, 15].

3.1. C_3N_4 polymorphs

Non-Graphitic Phases – structural property: An account of α, β, γ (spinel), and cubic phases of C_3N_4 has been presented earlier [12, 18]. The structures are shown in Fig. 2. The α-C_3N_4 phase (Fig. 2(a)) consists of the corner sharing CN_4 tetrahedron along with

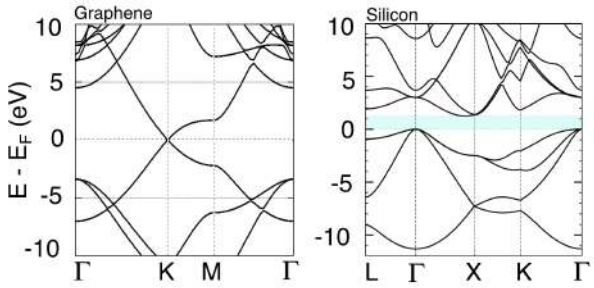

Figure 1: FP-NMTO-LDA+vLB calculated band-structure of 2D-graphene (left) and bulk-Si (right). The predicted Dirac-point in 2D-graphene (K-point) [45] and band gap of bulk-Si (1.25 eV) is in good agreement with experiment (1.17 eV) [29] and other theory [25].

pyramidal NC_3 in spheroidal cavities, suggesting that C and N are sp^3 and sp^2 hybridized, respectively [12]. The α-phase has 4 formula units (f.u.) per cell with 28 atoms. The β-C_3N_4 (Fig. 2(b)) has 6-, 8- and 12-membered rings of alternating C and N atoms [18]. The β-phase has two inequivalent N atoms: (I) one N has three equidistant nearest carbon atoms with the C-N-C angles ~120°, which shows that the C and N are sp^2 hybridized; and (II) other N is bonded to three non-planar carbon atoms in sp^2-sp^3 fashion. The γ-phase (Fig. 2(c)) has a spinel structure, which is known as cubic-modification of boron-nitride (c-BN) [48]. Two carbon atoms bond octahedrally to six nitrogen atoms, while the third carbon atom bonds tetrahedrally to four nitrogen atoms [49]. The tetrahedrally and the octahedrally bonded C-N are arranged alternatively in a 1:2 ratio. These are sequentially connected to one another at the N−corners. The cubic-C_3N_4 (Fig. 2(d)) is a high-pressure modification of Willemite mineral (Zn_2SiO_4) [12], formed by replacing the O with N and Zn and Si with C of Zn_2SiO_4 structure, so N and C are sp^3 hybridized.

The structural properties of C_3N_4 polymorphs are summarized in Table. 1. The PBE, PBEsol and LDA+vLB calculated structural parameters are in good agreement [50, 51]. Our predicted lattice constants are similar to those of experiment for α (a=6.5680 Å, c=4.7060 Å) and β phases (a=6.4017 Å, c=2.4041 Å) [50, 52]. We also evaluate bulk moduli by fitting lattice constant versus total energies to the Birch-Murnaghan equation of state [53, 54], which indicates that C_3N_4 undergoes uniform compression under applied hydrostatic pressure. The agreement between LDA+vLB and PBEsol calculated numbers establishes effectiveness and the utility of vLB-modified XC functional [19]. The electronic and optical property calculations are carried out using optimal lattice parameters

Polymorphs	α $P3_1c$ (159)			β $P6_3/m$ (176)				γ $Fd\bar{3}m$ (227)			Cubic $I\bar{4}3d$ (220)		
XC→	vLB	PBE	PBEsol	vLB	PBE	PBEsol	Expt.	vLB	PBE	PBEsol	vLB	PBE	PBEsol
a (Å)	6.4000	6.5350	6.4945	6.4100	6.4538	6.4177	6.4017	6.7824	6.7867	6.7350	5.4410	5.4496	5.4169
c (Å)	4.6296	4.7382	4.7099	2.4537	2.4243	2.4103	2.4041	-	-	-	-	-	-
a/c	1.3824	1.3792	1.3789	2.6124	2.6621	2.6626	2.6628	-	-	-	-	-	-
V (Å^3)	165.766	175.242	172.041	87.311	87.450	85.973	-	77.999	78.149	76.375	80.539	80.958	79.510
ρ (gm/cm^3)	3.6887	3.4893	3.5542	3.6114	3.4961	3.5562	-	3.9197	3.9122	4.0031	3.7962	3.7765	3.8452
B_0 (GPa)	452.676	419.362	453.841	590.139	413.894	440.825	-	421.482	391.717	421.015	469.360	442.050	467.965

Table 1: Comparison of lattice constants and bulk moduli of C_3N_4 polymorphs calculated using vLB, PBE and PBEsol functionals. Experimental lattice constant of β phase [50] are compared with calculated values. Bulk moduli calculated with vLB and PBEsol are in good agreement.

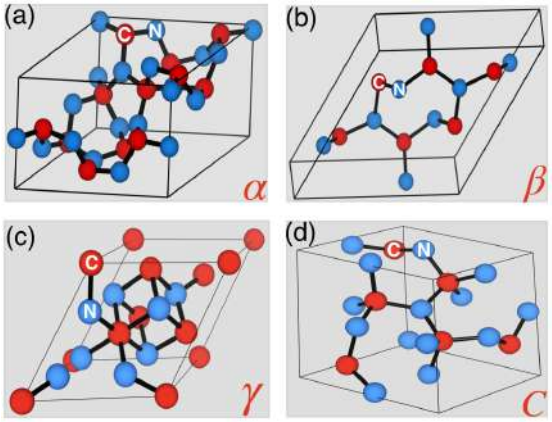

Figure 2: Crystal structure of carbon-nitride (C_3N_4) polymorphs: (a) α-phase (trigonal; space group:$P3_1c$;159); (b) β-phase (hexagonal; $P6_3/m$; 176); (c) γ-phase (spinel; $Fd\bar{3}m$; 227); (d) C-phase (cubic; $I43d$; 220). See phase stability in Fig. S3.

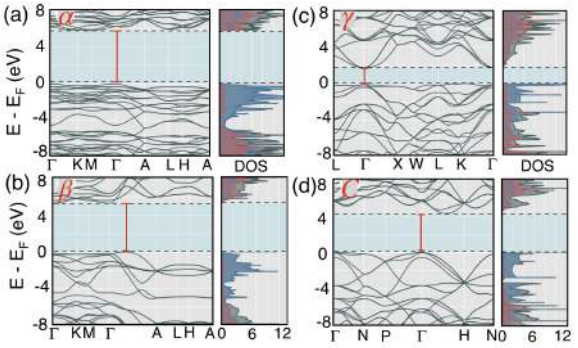

Figure 3: Electronic dispersion and DOS of C_3N_4 polymorphs: (a) α; (b) β; (c) γ, and (d) C phases. All phases show indirect gaps, except for γ. C (red line) and N (blue line) projected DOS are shown.

given in Table. 1.

Non-Graphitic Phases – electronic structure: Band structure is one of the most stringent tests to detail the materials physics. For example, Si, calcite and Cu have similar electron densities, but they have very different physical and electronic properties. This drives us to understand the band structure versus energy of C_3N_4 polymorphs in detail, shown in Fig 3 with a zero of energy at the VBM (E_F). The LDA+vLB band gaps for α, β, γ and cubic (C) phases are 5.81, 5.32, 1.81 and 4.23 eV, respectively. The band gaps of α, β and C phases are indirect in nature, while γ phase shows a direct gap. We find good agreement between our predictions and more advanced DFT techniques (e.g., HSE and G_0W_0), see Table. 2.

The projected and total density of states (DOS) of N and C are shown in Fig. 3 for each of the C_3N_4 polymorphs. In Fig. 3 (a), for the α phase the valence bands (VBs) below −4 eV phase are dominated by both N and C, while, the bands from −4 eV to E_F are mostly from N. This suggests that the electrons of N are loosely bound than those of C. The α phase has a wider band gap, and steeper VB and CB edges, compared to the others. The VB maxima and CB minima in α phase are at Γ and M point, respectively. Similar to α, we find that β (Γ − A to Γ) and C (Γ to Γ − H) are indirect band gap semiconductor with no contribution from C bands near E_F. However, the γ phase is a direct (Γ-Γ) band gap with minor contribution from C bands near E_F. The electronic structures of α, β, γ and cubic polymorphs split to form the separate VB, which reflects the presence of smaller asymmetric part of the potential. The presence of asymmetric potential is the reason behind the stronger mixing of low lying N and C states.

Graphitic Phases – structural property: Notably, graphitic phases of C_3N_4 are considered for next generation visible-light-driven metal-free, non-toxic, earth-abundant semiconductors, which can find applications in energy conversion, hydrogen evolution, sensing and imaging [1]. Earth-abundant graphitic C_3N_4 possesses excellent electronic band structures, electron-rich properties, and higher stability. The sp^2 hybridized planar graphitic C_3N_4 (Space group: $P6m2$; #187) in Fig. 4 can be viewed as graphite whose C lattices are partially

	Band Gap (eV)									
C_3N_4	Expt.	This Work				Others				
Polymorphs		LDA	PBE	vLB	HSE	LDA [16–18, 55, 56]	PBE	HSE[57]	*GW*[56]	mBJ[58]
α	–	5.24*	–	5.81	5.81	3.8-3.85	–	–	5.49	–
β	–	3.27	3.31	5.32	5.34	3.11-3.56	–	–	4.85, 6.4[55]	–
γ	–	1.19	1.14	1.81	1.95	–	–	–	2.01 **(this work)**	–
cubic	–	2.86	2.95	4.23	4.43	2.90-2.91	–	–	4.30	–
$t-g(AA)$	3.1[59]	2.79	2.70	3.02	3.21	1.16-1.48,0.699[58]	0.870[58]	3.19	2.97	2.549
$t-g(AB)$	–	2.66	2.67	2.95	3.39	1.204[58]	1.357[58]	–	–	2.99
$h-g$	2.67-2.95 [1, 2, 8, 16, 60]	–	–	2.71	2.71	–	–	2.772	2.88	–

Table 2: Calculated band gaps for C_3N_4 polymorphs using (LDA, PBE, vLB, HSE) and comparison with other theories [16–18, 55–58] (LDA, PBE, HSE, GW, mBJ) and experiments [1, 2, 8, 16, 59]. HSE calculations are done with plane-wave basis.[31, 32] Band gaps using vLB [19] and HSE (this work) shows good agreement with existing HSE, GW and experiments. We also include non-self-consistent GW band gap for γ-C_3N_4 phase calculated with QE package. Band gaps from HSE (1.95 eV), GW (2.01 eV) and vLB+LDA (1.81 eV) are in good agreement.

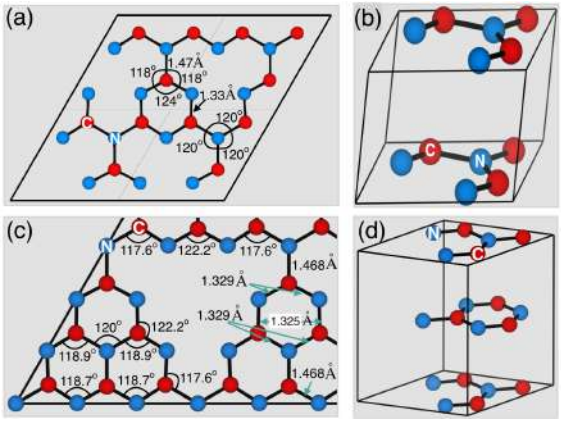

Figure 4: Crystal structure of relaxed graphitic-C_3N_4: (a) $t-g$(AA), (b) $t-g$(AA) unit cell, and (c) $h-g$(AA), (d) $t-g$(AB) unit cell C_3N_4. For relaxed $t-g$ phase, bond angles and lengths vary from ($118-124^o$) and ($1.33-1.47$ Å), respectively, while, in relaxed $h-g$ phase, bond angles and lengths vary as ($117.6-122.2^o$) and ($1.325-1.468$ Å).

substituted with nitrogen (in regular fashion) [1]. We prepare triazine with (AA; AB) stacking and heptazine with AA stacking, respectively. The large cavities in t-g(AA), t-g(AB) and h-g(AA) allow neighboring atoms to relax and lead to increased bond lengths and angles compared to other phases (Fig. 4). For t-g(AA), the equilibrium lattice constants are $(a, c) = 4.786, 3.758$ Å, where bond lengths and angles vary from $(1.327-1.463$ Å) and $(118-124^o)$, respectively. The calculated inter-layer spacing of 3.505 Å and lattice constant of t-g(AB) $(a, c) = (4.784, 7.007)$ Å is in good agreement with experiment ($(a, c) = (5.041, 6.576)$ Å) [61]. The bond lengths vary from $1.326-1.468$ Å, while the angles range from $117.6-122.2^o$. Due to larger cavity size compared to t-g(AA) and t-g(AB), the h−g (AA) structure shows larger degree of relaxation, both in bond lengths and angles as shown in Fig. 4(d).

Graphitic Phases – electronic structure: Experimentally thin films of graphitic-C_3N_4 can be produced on different substrates. By controlling the synthesis conditions, the band gap can be tuned from 2.65 to 3.1 eV, which falls in the range of visible light [1, 16, 59]. The LDA+vLB band gap of 3.02 eV for AA (trigine) and 2.95 eV for AB (heptazine) stackings are in close agreement with experimental gap (3.1 eV) [59]. The QE-HSE predicted band gap for AA and AB stackings is 3.21 eV and 3.39 eV, respectively. LDA+vLB predicted band gaps are in excellent agreement with HSE, other theory [56, 57], and other experiments. The t-g(AA) shows indirect (K−A) band gap, whereas t-g(AB) is direct. The LDA+vLB predicted indirect (Γ-M) band gap (2.71 eV) of h-g-C_3N_4 is in good agreement with HSE (2.71 eV), other theory [56, 57], and experiments $2.67-2.95$ eV [1, 2, 8, 16, 60].

To identify active sites in C_3N_4 polymorphs, we plot the CBM and VBM charge densities (Fig. 5, right-panel). The CBM of $t-g$(AA), $t-g$(AB) and $h-g$(AA) C_3N_4 are mainly composed of N-2p and C-2p states, while the VBM is dominated by N-2p states. Also, strongly localized CBM and VBM states in charge density plots suggest the possibility of low photo-absorption efficiencies, i.e., $e^- - h^+$ excitation under visible-light irradiation occuring on the edge of N and C atoms.

In Table 2, we compare the calculated band gaps from LDA, PBE, vLB, and HSE (present work) with other theory and experiments [1, 8, 16, 16–18, 55–60]. The LDA+vLB and QE-HSE predicted band gap for cubic phase is in good agreement with GW, while band gap for α and β phase is higher than GW.

3.2. Effective mass – C_3N_4 polymorphs

The dynamical activity of the charge careers in semiconductor depends on its mobility, which is inversely proportional to the effective mass (m^*). Near the band edges, effective mass is described by $m^* = \hbar^2/\left(\frac{d^2E}{dk^2}\right)$, where $\frac{d^2E}{dk^2}$ is the band-curvature at VBM for holes and

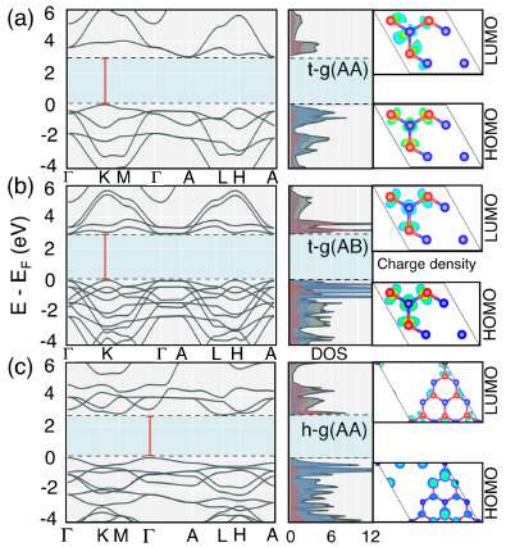

Figure 5: Electronic band-structures, density of states and charge densities (VBM & CBM states) of relaxed graphitic-C_3N_4– (a) $t-g$(AA), (b) $t-g$(AB), and (c) $h-g$(AA). The $t-g$(AA), $t-g$(AB) and $h-g$(AA) phases exhibit band gaps of 3.02 eV (K–A; indirect), 2.95 eV (Γ – Γ; direct) and 2.71 eV (Γ-M; indirect), respectively. C-p (red) and N-p (blue) projected density of states (PDOS) are shown. Charge-density isosurface plots are set at 0.035 electrons/Å^3.

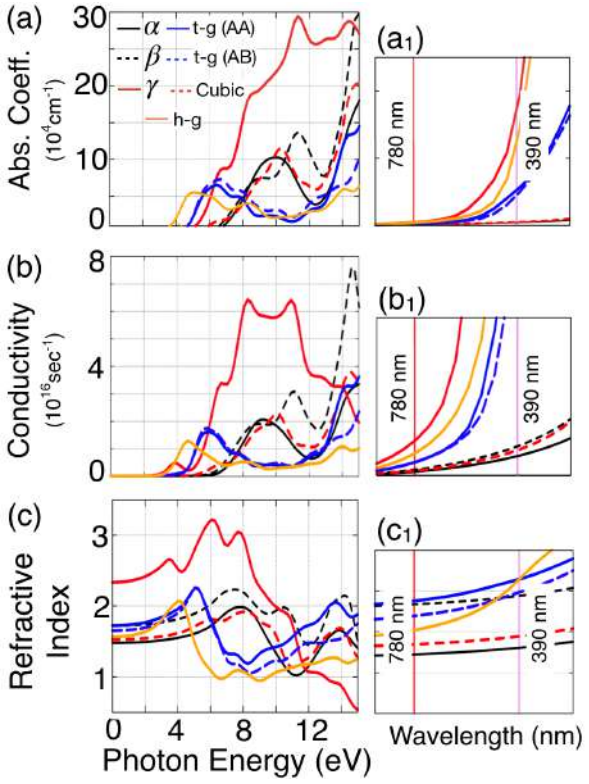

Figure 6: QE-HSE calculated (a) Absorption spectra, (b) optical conductivity, and (c) refractive index vs. photon energy for C_3N_4 polymorphs. (a_1) Absorption spectra, (b_1) optical conductivity, and (c_1) refractive index are also shown in the visible region of light.

at CBM for electrons. The m* for C_3N_4 polymorphs is shown in Table 3. The calculated m* in graphitic phase is in good agreement with the available results [62, 63] and we find electron m* of γ phase is much lower than graphitic phases. This indicates that the electron mobility in γ phase is easier. Interestingly, between the two types of stacking in t-graphitic phases, the A-B alternate stacking provides lower electron and hole effective mass and higher mobility than the AA phase. We attribute this to the lower symmetry of AB phase.

Polymorphs	**m***	
	e$^-$	**h$^+$**
α	0.045	-0.050
β	0.022	-0.137
γ	0.016	-0.065
cubic	0.039	-0.065
$t-g(AA)$	0.044	-0.044
$t-g(AB)$	0.028	-0.026
$h-g(AA)$	0.045	-0.081

Table 3: Effective mass (m*) of C_3N_4 polymorphs in electron rest mass (m_0) units.

3.3. Optical Properties:

Solar energy output is mostly dominated by: (I) ultraviolet (~5%), visible (~45%), and infrared (~50%) region of electromagnetic wave spectrum [64]. The visible-light photocatalysis therefore offers the best opportunity to utilize maximum solar energy [65]. Except for γ and $h-g$, the C_3N_4 polymorphs possess relatively wide band gaps (see Table. 2). The optimal gap of γ and $h-g$ C_3N_4 [66] makes them promising polymeric semiconductors suited for visible-light absorption.

In Fig. 6, we plot absorption coefficient, optical conductivity, and refractive index vs photon energy. Plots of effective number of electrons participating in interband transition (n_{eff}) shows that the (0–15 eV) range of photon energy is justified (Fig. S4). However, our region of interest is visible light from 1.59 eV (780 nm) to 3.18 eV (390 nm), in Fig. 6 (a_1, b_1, c_1). The optical spectra (obtained from the imaginary part of the dielectric function) contains the information of character and number of occupied and unoccupied bands. These together decide the accuracy of optical properties at higher excita-

tion energies.

The absorption coefficient of a material determines the spatial region in which most of the light is absorbed. The absorption edge extent of the γ and $h-g$ phases is relatively larger than other polymorphs due to narrower gaps of 1.81 and 2.71 eV, respectively [66]. The onset of absorption for γ and $h-g$ phases are located at roughly 2.0 and 3.0 eV, respectively, very close to the their band gaps. Also, the structural change induced by relaxation in Fig. 4(d) for h-g are manifested by more pronounced changes in the optical absorption in Fig. 6(a)&(a1) (AA) as compared to t-g (AA) and t-g (AB). The degree of relaxation and band gap decides the absorption-onset (AO) and band-edge absorption (BE), for example, for h-g phase BE/AO is at 3.0 eV smaller than t-g(AA) and t-g(AB). Interestingly, both γ and $h-g$ phases show an increase in optical absorption range. However, the γ phase shows enhanced light absorption in the whole spectral region due to direct nature of its band gap. Also, direct gap materials provide better photons to electron-hole pair conversion useful for efficient electro-optical devices – the foremost reason behind higher optical absorbance in γ phase, as shown in Fig. 6(a).

The accurate description of the band gap and band-positions from hybrid-functionals assure the reliability of our prediction of optical properties. We compared the QE-HSE calculated optical conductivity of C_3N_4 polymorphs in Fig. 6(b). Our results shows that the conductivity starts with a gap, indicating the semiconducting character of each polymorph. The optical conductivity is zero below a certain energy value, which is consistent with the respective band gaps in Table 2 of C_3N_4 polymorphs. The optical conductivity for the γ phase in Fig. 6(b) is slightly higher than $h-g$ phase, which is related to absorption coefficient (Fig. 6(a)) and shows similar behavior in the range of visible light (1.59 to 3.18 eV). Only in the energy range of 4 to 5.5 eV does other polymorphs overtake γ, whereas it shows large jump in absorption and conductivity beyond photon energy 5.5 eV. The increased optical conductivity in visible light range makes of γ phase a promising candidate for photovoltaic application. Refractive index is shown in Fig. 6(c) as a function of photon energy (wavelength: in Fig. 6 (a_1, b_1, c_1)). Physically the calculated optical gap corresponds to the photon energy at which the imaginary part of the refractive index, k, becomes non-zero. We found that the refractive index for C_3N_4 polymorphs vary from 1.4 to 1.9 for the visible range of light 390 – 780 nm, showing sensitivity of the refractive indices to crystal structure. The optical absorption spectra are directly connected to the imaginary part of the refractive index, see Eq. (4). So, the peaks and valleys in refractive index are expected in the similar energy range that of absorption spectra.

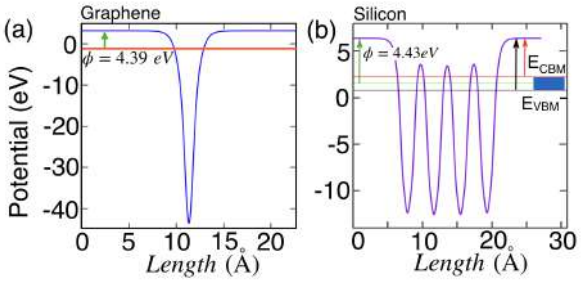

Figure 7: QSE-HSE calculated work-function of (a) 2D-graphene (4.39 eV), and (b) bulk-Si (4.43 eV) is in good agreement with experiments (2D-graphene, 4.56 eV [33]; bulk-Si, 4.87 eV [34]).

3.4. Work Function

Monolayer graphene and bulk-Si: The work function, which limits the performance of devices, is an important characteristics of semiconductors that should be taken into considerations. First, we cross-validate QE-HSE method by calculating work-function of well-studied 2D-graphene, and bulk-Si. The $3\times3\times1$ and $2\times2\times1$ supercells are chosen for accurate calculations of 2D-graphene and bulk-Si, respectively. The inter-slab vacuum of 15 Å is chosen along (001) to avoid periodic image problem. In Fig. 7a, we show the calculated work-function of 4.39 eV for 2D-graphene. The ϕ_{DFT} is in good agreement with ϕ_{Expt}=4.56 eV [33]. In Fig. 7b, the conduction-band minima (CBM) and valence-band maxima (VBM) for Si are plotted considering E_{vac}= 0. The calculated work-function of 4.43 eV for Si is in very good agreement with experiments (4.87 eV) [34].

C_3N_4 polymorphs: At ambient conditions (i.e., at normal (room) temperature and one atmospheric pressure), the thermodynamic voltage for water splitting is 1.23 V [67, 68]. But, to supply the required photo-voltage, a photo-electrochemical cell with single illuminated electrode needs gaps greater than 1.6 eV [69]. In Table 2, we show that the gap in γ and graphitic phases is suitable for photoabsorption. To initiate water-redox reaction in semiconductors, optimal gaps, as well as band-edge (conduction and valence) positions of VBM and CBM states are important. The valence-band maxima should be more positive (E_{H_2O/O_2}=1.23, 0.81 V for pH=0, 7) with respect to normal hydrogen electrode (NHE) than the water oxidation level, whereas the conduction-band minima should be more negative (E_{H^+/H_2}=0, −0.41 V for pH=0, 7 vs. NHE) than the

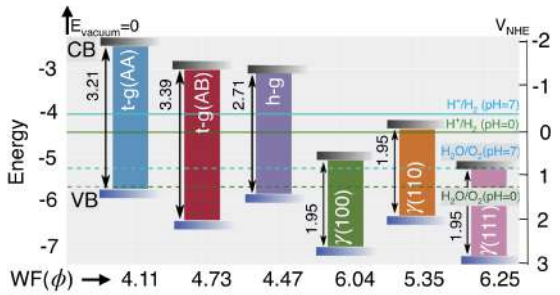

Figure 8: Conduction and valence band positions of C_3N_4 polymorphs with respect to water reduction and oxidation potentials.

H-production potential:

$$\begin{aligned} H_2O + 2h^+ &\rightarrow 2H^+ + \frac{1}{2}O_2 \\ 2H^+ + 2e^- &\rightarrow H_2 \quad . \end{aligned} \tag{8}$$

In Fig. 8, we illustrate valence and conduction band positions and work function for $t-g$(AA), $t-g$(AB), $h-g$, and γ phase for (100), (110) and (111) planes. The VBM for graphitic phase is positive with respect H_2O/O_2 -p_H = 0 level while CBM are negative compared to $H^+/H_2 - p_H = 0$ level in the entire pH-range (0 to 7). The work function of the triazine phases depends largely on the choice of stacking: alternate (AB) stacking increases the band gap and also enhances the work-function potential. The band-position in both t-g (AA) and t-g (AB) makes them good candidate for photocatalysis, however, t-g (AB) is more favorable due to larger work function in the entire pH range. The QE-HSE predicted $h-g$ C_3N_4 work function (4.47 eV) agrees well with the experiments (4.3 eV) [70, 71]. For $h-g$-C_3N_4, Yu *et al.* [72] showed that the band gap range of 2.44-2.69 eV and VBM at 1.50 eV with respect to NHE at room temperature, in good agreement with our predicted band gap of 2.71 eV and VBM at 1.385 eV. The CBM and VBM positions in Fig. 8 suggests that graphitic-C_3N_4 favors water (pH = 7) over acidic water (pH < 7) for photocatalysis.

γ-C_3N_4 workfunction: Our ability to modulate the work function of semiconductor alloys, e.g., through control of surface orientation, is an enabling factor. The optimal band gap (1.95 eV) for γ-phase makes it more efficient for the photo-absorption in visible spectra compared to other C_3N_4 polymorphs. Among the three illuminated surface conditions of γ phase, i.e., (100), (110), (111) (see Fig. S5 in supplement), the VB and CB band range of (110) surface is favorable at pH=0. Our study suggest γ-C_3N_4 as a potential candidate for photocatalytic application, a new and efficient photocatalysts from spinel group [73].

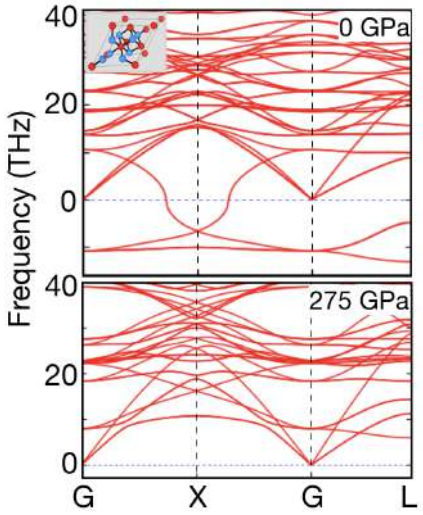

Figure 9: Phonon dispersion in γ-C_3N_4 along high-symmetry directions. (Top) Modes at 0 GPa shows dynamical instability, i.e., imaginary frequencies denoted by negative values. (Bottom) With pressure unstable modes disappear at/above the critical pressure of 275 GPa, with a 11.5% volume change compared to zero pressure.

3.5. Pressure effect on key properties of γ-C_3N_4:

Optimal band gap (1.95 eV) for γ-phase indicates its suitability for optical and photocatalytic application. Yet, most C_3N_4-polymorphs suffer from structural instabilities [74, 75], i.e., all these have phonons with imaginary frequencies at zero applied pressure. It is noteworthy that metastable γ-C_3N_4 is already been experimentally observed by Andrade *et. al.* [76]. The measurements found the emission signals for γ-C_3N_4 , but signals disappear after few scanning tunneling microscopy (STM) scans. As the experiments were performed at atmospheric conditions, where oxygen is always present and STM scans can generate high-energy photons, which possibly oxidizes the γ-C_3N_4 phase. This indicates towards metastability of γ-C_3N_4 at ambient conditions (i.e., at room temperature and one atmospheric pressure). Therefore, we investigate the pressure effect on γ-phase. In Fig. 9, we plot phonons at 'zero' pressure (top) and at 275 GPa (bottom). The 0 GPa phonons show imaginary frequencies that indicates a dynamical instability in γ-phase. However, under hydrostatic pressure (above 275 GPa) all imaginary frequencies in Fig. 9 disappear, i.e., above a critical pressure γ-phase become dynamically stable.

The dynamically stable γ-phase also satisfies the Born stability criteria [77], i.e., (a) $C_{11} - C_{12} > 0$; (b)

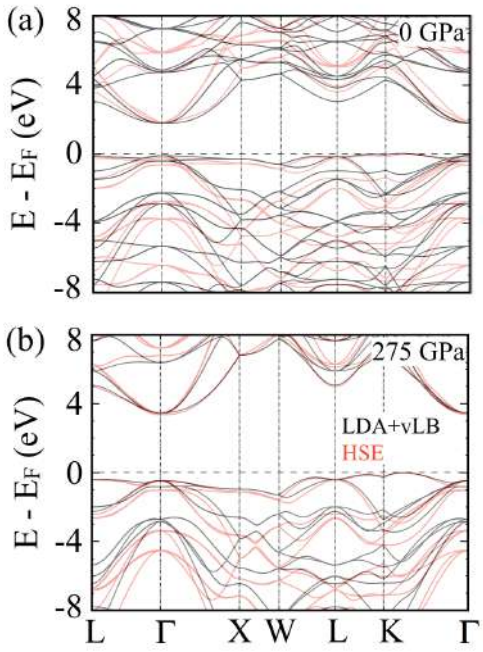

Figure 10: The LDA+vLB and QE-HSE calculated electronic band-structures of γ-C_3N_4 at (a) 0 GPa, and (b) 275 GPa. The shape and position of conduction band minima and valence band maxima calculated using LDA+vLB and QE-HSE for γ-C_3N_4 in (a) and (b) shows good agreement.

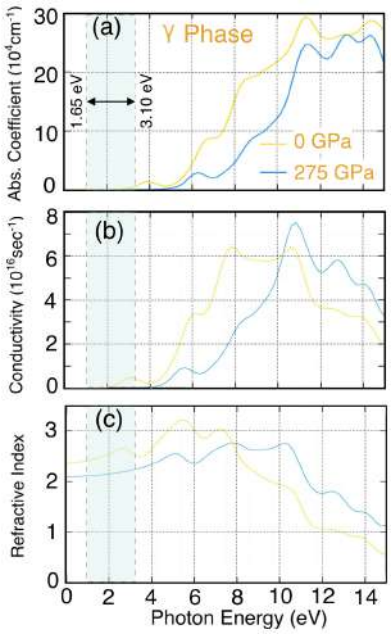

Figure 11: (a) Absorption spectra, (b) optical conductivity, and (c) refractive index versus photon energy for γ-C_3N_4 at 'zero' pressure (yellow) and 275 GPa (blue) calculated using HSE functional. The shaded zone indicates visible light range (1.65−3.10 eV).

$C_{11} + 2C_{12} > 0$; (c) $C_{44} > 0$, where C_{11} = 436.5 GPa, C_{12} = 363.09 GPa, and C_{44} = 446.5 GPa. The strong covalent bonding gives large bulk-, elastic-, and shear-modulus of 387.6 GPa, 682.0 GPa and 282.6 GPa, respectively.

To point out the effect of pressure on band-structure, we plot electronic band-structures of γ-C_3N_4 in Fig. 10(a)&(b). For with and without pressure cases, γ-C_3N_4 shows good agreement for conduction band minima and valence band maxima positions, which is important both for calculation of optical properties and band alignment in determining photocatalytic behavior.

The effect of pressure clearly reflects on optical properties of γ-C_3N_4 (Fig. 11). We found an increase in the extent of absorption edge for the γ phase compared to ambient (one atmospheric) pressure (Fig. 11(a)). The absorption edges at ~300 nm for γ phase corresponds to the band gap energy of 3.43 eV. First, the optical absorption range for γ phase increases under pressure, and, secondly, the optical conductivity of γ-C_3N_4 (Fig. 11(b)) also changes from that at "zero pressure" (Fig. 6(b)). A slight change in conductivity compared to "zero-pressure" suggests increased photocatalytic behavior of γ-phase. Refractive index of dynamically stable γ-phase in Fig. 11(c) reduces compared to "zero pressure" case. The calculated optical gap corresponds to the photon energy at which the imaginary part of the refractive index, k, becomes non-zero. We find the refractive index for γ-C_3N_4 changes 2.5 to 2.05 for the visible light range.

In Fig. 12, we compare the VB and CB positions and work function for most favorable surface (110) of γ phase with(out) pressure. Clearly, the photocatalytic range of γ (110)-surface under pressure (275 GPa) increases. We also showcase the effect of water on (110) surface on γ phase and find slight reduction in CB band-edge compared to surface with no water. The CB band-edge becomes slightly less positive compared to pure (110) surface, whereas, the γ (110) phase is now more favorable under pressure due to increased photocatalytic range (pH=0 to 7) in both with and without water case.

The pressure profile for the structural stability of γ-C_3N_4 is significantly higher, however, recent studies presented novel and more practical synthesis routes for new or known high-pressure phases under predictable nonhydrostatic loading [78]. It has been exemplified for silicon that the hydrostatic pressure of 76 GPa could be lowered by 21 times to 3.7 GPa under uniaxial loading. We believe that the similar idea could be employed in future for synthesizing new high-pressure carbon-

nitride materials. To add further discussion on pressure and point out its importance, recently, pressure has helped discover new material(s) and mechanisms [79, 80]. Although, the stability of γ-C_3N_4 is an issue [81, 82], the use of hydrostatic pressure in this work is an effort to provide theoretical understanding of metastable (structurally unstable) γ-C_3N_4.

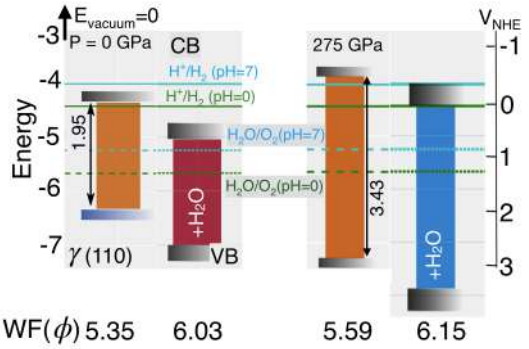

Figure 12: At 0 GPa (dynamically unstable) and 275 GPa (stable), the conduction and valence band positions of favorable (110) surface with and without water of $\gamma - C_3N_4$-polymorph with respect to water reduction and oxidation potentials.

4. Conclusion

We present a detailed study of both structural and electronic-structure of C_3N_4 polymorphs using a localized-basis (FP-LMTO-LDA+vLB) and a plane-wave basis (QE-HSE) method. The structural properties and band gap of C_3N_4-polymorphs predicted from LDA+vLB agrees well with our more accurate QE-HSE results, and available experiments. We did cross-validation tests performed on two diverse cases: (a) 2D-graphene, and (b) bulk-Si. The calculated band gaps (graphene, 0 eV; bulk Si, 1.25 eV indirect) agree well with experiments, which shows the predictive reliability and accuracy. To point out important differences between our approach and other calculations done for C_3N_4 in literature are two-fold, (a) most calculations are performed using LDA/GGA functionals, which are known to underestimate the band gap; and (b) hybrid or GW functionals were not used in systematic way to study of relevant governing factors for photocatalytic performance of carbon-nitrides.

We performed optical-property, and work-function calculation using hybrid-functional (HSE) as implemented within Quantum-Espresso package. Beside lattice parameters and band gaps, work-function calculations are found to be in very good agreement with the available experiments. Our calculations show optimal band gap of 1.95 eV as well as higher optical conductivity and carrier mobility for γ-C_3N_4 than other polymorphs, which makes γ-C_3N_4 a suitable candidate for photocatalytic applications. The work function in γ-C_3N_4 shows an orientation dependence with (110) surface as most favorable orientation over (100) and (111). In spite of favorable electronic-structure and optical properties, γ-phase shows a dynamical instability (unstable phonons) at standard temperature and pressure. We show that γ-C_3N_4 is structurally stabilized under hydrostatic pressure (275 GPa) and leads to a significant improvement in photocatalytic behavior with respect to water reduction and oxidation potentials. We could also identify the active sites in C_3N_4-polymorphs from charge-density plots as strongly localized states, usually suggesting low photo-absorption efficiencies. Our study offers γ phase as a new candidate to explore for optical and photocatalytic applications, which may further ignite interest in C_3N_4 polymorphs within the materials and chemistry community.

ACKNOWLEDGMENT

SD and PS equally contributed. vLB routines for TB-LMTO-ASA and FP-NMTO are developed by PS/MKH/DDJ and SD/AM, respectively. Calculations are carried out by SD/DJ/CBC in collaboration with PS/DDJ. Research at Ames Laboratory was supported by the U.S. Department of Energy (DOE), Office of Science, Basic Energy Sciences, Materials Science and Engineering Division. Ames Laboratory is operated for the U.S. DOE by Iowa State University under Contract No. DE-AC02-07CH11358.

References

[1] X. Wang, K. Maeda, A. Thomas, K. Takanabe, G. Xin, J. M. Carlsson, K. Domen and M. Antonietti, Nature materials, 2009, **8**, 76–80.
[2] X. Wang, K. Maeda, X. Chen, K. Takanabe, K. Domen, Y. Hou, X. Fu and M. Antonietti, Journal of the American Chemical Society, 2009, **131**, 1680–1681.
[3] K. Li, X. Xie and W.-D. Zhang, Carbon, 2016, **110**, 356–366.
[4] C. Hu, Y.-R. Lin and H.-C. Yang, ChemSusChem, 2019, **12**, 1794–1806.
[5] J. Fu, J. Yu, C. Jiang and B. Cheng, Advanced Energy Materials, 2018, **8**, 1701503.
[6] B. Zhu, L. Zhang, B. Cheng and J. Yu, Applied Catalysis B: Environmental, 2018, **224**, 983–999.
[7] X. Ma, Y. Lv, J. Xu, Y. Liu, R. Zhang and Y. Zhu, The Journal of Physical Chemistry C, 2012, **116**, 23485–23493.
[8] G. Liu, C. Y. Jimmy, G. Q. M. Lu and H.-M. Cheng, Chemical Communications, 2011, **47**, 6763–6783.
[9] F. Shayeganfar and R. Shahsavari, Carbon, 2016, **99**, 523–532.
[10] D.-H. Lan, H.-T. Wang, L. Chen, C.-T. Au and S.-F. Yin, Carbon, 2016, **100**, 81–89.

[11] X. Li, J. Yu, J. Low, Y. Fang, J. Xiao and X. Chen, Journal of Materials Chemistry A, 2015, **3**, 2485–2534.
[12] D. M. Teter and R. J. Hemley, Science, 1996, **271**, 53–55.
[13] Y. Guo and W. A. Goddard, Chemical Physics Letters, 1995, **237**, 72–76.
[14] J. P. Perdew, K. Burke and M. Ernzerhof, Physical Review Letters, 1996, **77**, 3865–3868.
[15] J. Perdew, Phys. Rev. Lett., 2008, **100**, 136406.
[16] M. Mattesini, S. F. Matar and J. Etourneau, Journal of Materials Chemistry, 2000, **10**, 709–713.
[17] H. Yao and W. Ching, Physical Review B, 1994, **50**, 11231.
[18] B. Molina and L. Sansores, Modern physics letters B, 1999, **13**, 193–201.
[19] P. Singh, M. K. Harbola, M. Hemanadhan, A. Mookerjee and D. D. Johnson, Phys. Rev. B, 2016, **93**, 085204.
[20] R. V. Leeuwen and E. J. Baerends, Physical Review A, 1994, **49**, 2421–2431.
[21] O. Jepsen, http://www.mpi-stuttgart.mpg.de/andersen/, 2000.
[22] Y. Nohara and O. Andersen, Physical Review B, 2016, **94**, 085148.
[23] F. Tran and P. Blaha, Phys. Rev. Lett., 2009, **102**, 226401.
[24] S. Datta, P. Singh, C. B. Chaudhuri, D. Jana, M. K. Harbola, D. D. Johnson and A. Mookerjee, Journal of Physics: Condensed Matter, 2019, **31**, 495502.
[25] P. Singh, M. K. Harbola, B. Sanyal and A. Mookerjee, Phys. Rev. B, 2013, **87**, 235110.
[26] P. Singh, M. Harbola and A. Mookerjee, in Modeling, Characterization, and Production of Nanomaterials, Elsevier, 2015, pp. 407–418.
[27] P. Singh, M. K. Harbola and D. D. Johnson, Journal of Physics: Condensed Matter, 2017, **29**, 424001.
[28] B. Sadhukhan, P. Singh, A. Nayak, S. Datta, D. D. Johnson and A. Mookerjee, Phys. Rev. B, 2017, **96**, 054203.
[29] J. W. Precker and M. A. da Silva, American Journal of Physics, 2002, **70**, 1150–1153.
[30] J. Heyd and G. E. Scuseria, The Journal of chemical physics, 2004, **121**, 1187–1192.
[31] P. Giannozzi, S. Baroni, N. Bonini, M. Calandra, R. Car, C. Cavazzoni, D. Ceresoli, G. L. Chiarotti, M. Cococcioni, I. Dabo, A. D. Corso, S. de Gironcoli, S. Fabris, G. Fratesi, R. Gebauer, U. Gerstmann, C. Gougoussis, A. Kokalj, M. Lazzeri, L. Martin-Samos, N. Marzari, F. Mauri, R. Mazzarello, S. Paolini, A. Pasquarello, L. Paulatto, C. Sbraccia, S. Scandolo, G. Sclauzero, A. P. Seitsonen, A. Smogunov, P. Umari and R. M. Wentzcovitch, Journal of Physics: Condensed Matter, 2009, **21**, 395502.
[32] P. Giannozzi, O. Andreussi, T. Brumme, O. Bunau, M. B. Nardelli, M. Calandra, R. Car, C. Cavazzoni, D. Ceresoli, M. Cococcioni, N. Colonna, I. Carnimeo, A. D. Corso, S. de Gironcoli, P. Delugas, R. A. DiStasio, A. Ferretti, A. Floris, G. Fratesi, G. Fugallo, R. Gebauer, U. Gerstmann, F. Giustino, T. Gorni, J. Jia, M. Kawamura, H.-Y. Ko, A. Kokalj, E. Küçükbenli, M. Lazzeri, M. Marsili, N. Marzari, F. Mauri, N. L. Nguyen, H.-V. Nguyen, A. O. de-la Roza, L. Paulatto, S. Poncé, D. Rocca, R. Sabatini, B. Santra, M. Schlipf, A. P. Seitsonen, A. Smogunov, I. Timrov, T. Thonhauser, P. Umari, N. Vast, X. Wu and S. Baroni, Journal of Physics: Condensed Matter, 2017, **29**, 465901.
[33] D. Ziegler, P. Gava, J. Güttinger, F. Molitor, L. Wirtz, M. Lazzeri, A. Saitta, A. Stemmer, F. Mauri and C. Stampfer, Physical Review B, 2011, **83**, 235434.
[34] G. Hollinger and F. Himpsel, Journal of Vacuum Science & Technology A: Vacuum, Surfaces, and Films, 1983, **1**, 640–645.
[35] O. Andersen, C. Arcangeli, R. Tank, T. Saha-Dasgupta, G. Krier, O. Jepsen and I. Dasgupta, MRS Online Proceedings Library Archive, 1997.
[36] E. Kraisler and L. Kronik, The Journal of chemical physics, 2014, **140**, 18A540.
[37] C.-O. Almbladh and U. von Barth, Phys. Rev. B, 1985, **31**, 3231–3244.
[38] D. G. Anderson, J. ACM, 1965, **12**, 547–560.
[39] F. Wooten, Optical properties of solids, Academic press, 2013.
[40] N. Feng, F. Liu, M. Huang, A. Zheng, Q. Wang, T. Chen, G. Cao, J. Xu, J. Fan and F. Deng, Scientific reports, 2016, **6**, 34765.
[41] C. Fall, N. Binggeli and A. Baldereschi, Journal of Physics: Condensed Matter, 1999, **11**, 2689.
[42] A. Baldereschi, Phys. Rev. Lett., 1988, **61**, 734.
[43] N. E. Singh-Miller and N. Marzari, Physical Review B, 2009, **80**, 235407.
[44] A. Togo and I. Tanaka, Scr. Mater., 2015, **108**, 1–5.
[45] C. Soldano, A. Mahmood and E. Dujardin, Carbon, 2010, **48**, 2127 – 2150.
[46] S. Jana, A. Bandyopadhyay and D. Jana, Physical Chemistry Chemical Physics, 2019.
[47] M. T. Lusk and L. Carr, Carbon, 2009, **47**, 2226 – 2232.
[48] S.-D. Mo, L. Ouyang, W. Ching, I. Tanaka, Y. Koyama and R. Riedel, Physical Review Letters, 1999, **83**, 5046.
[49] J. Jiang, F. Kragh, D. Frost, H. Lindelov et al., Journal of Physics: Condensed Matter, 2001, **13**, L515.
[50] J. Z. Y. Tan, N. M. Nursam, F. Xia, M.-A. Sani, W. Li, X. Wang and R. A. Caruso, ACS Applied Materials & Interfaces, 2017, **9**, 4540–4547.
[51] L. Yang, P. W. May, L. Yin, J. A. Smith and K. N. Rosser, Journal of Nanoparticle Research, 2007, **9**, 1181–1185.
[52] Y. Qiu and L. Gao, Chemical Communications, 2003, 2378–2379.
[53] F. D. Murnaghan, Proceedings of the National Academy of Sciences, 1944, **30**, 244–247.
[54] F. Birch, Journal of Geophysical Research, 1952, **57**, 227–286.
[55] J. L. Corkill and M. L. Cohen, Physical Review B, 1993, **48**, 17622.
[56] Y. Xu and S.-P. Gao, International Journal of Hydrogen Energy, 2012, **37**, 11072–11080.
[57] M. Makaremi, S. Grixti, K. T. Butler, G. A. Ozin and C. V. Singh, ACS Applied Materials & Interfaces, 2018, **10**, 11143–11151.
[58] A. H. Reshak, S. A. Khan and S. Auluck, RSC Adv., 2014, **4**, 11967–11974.
[59] V. N. Khabashesku, J. L. Zimmerman and J. L. Margrave, Chemistry of materials, 2000, **12**, 3264–3270.
[60] Y. Wang, J. Zhang, X. Wang, M. Antonietti and H. Li, Angewandte Chemie International Edition, 2010, **49**, 3356–3359.
[61] G. Algara-Siller, N. Severin, S. Y. Chong, T. Björkman, R. G. Palgrave, A. Laybourn, M. Antonietti, Y. Z. Khimyak, A. V. Krasheninnikov, J. P. Rabe et al., Angewandte Chemie International Edition, 2014, **53**, 7450–7455.
[62] M. Dong, C. He and W. Zhang, Journal of Materials Chemistry C, 2017, **5**, 3830–3837.
[63] X. Li, Y. Dai, Y. Ma, S. Han and B. Huang, Physical Chemistry Chemical Physics, 2014, **16**, 4230–4235.
[64] J. A. Herron, J. Kim, A. A. Upadhye, G. W. Huber and C. T. Maravelias, Energy & Environmental Science, 2015, **8**, 126–157.
[65] P. Nath, S. Chowdhury, D. Sanyal and D. Jana, Carbon, 2014, **73**, 275–282.
[66] W. Shockley and H. J. Queisser, Journal of Applied Physics, 1961, **32**, 510–519.
[67] L. Meda and L. Abbondanza, Reviews in Advanced Sciences

and Engineering, 2013, **2**, 200–207.
[68] T. Jafari, E. Moharreri, A. Amin, R. Miao, W. Song and S. Suib, Molecules, 2016, **21**, 900.
[69] J. R. Bolton, S. J. Strickler and J. S. Connolly, Nature, 1985, **316**, 495.
[70] F. Yang, V. Kuznietsov, M. Lublow, C. Merschjann, A. Steigert, J. Klaer, A. Thomas and T. Schedel-Niedrig, Journal of Materials Chemistry A, 2013, **1**, 6407–6415.
[71] W.-J. Ong, L.-L. Tan, Y. H. Ng, S.-T. Yong and S.-P. Chai, Chemical reviews, 2016, **116**, 7159–7329.
[72] X. Yu, T. Fan, W. Chen, Z. Chen, Y. Dong, H. Fan, W. Fang and X. Yi, Carbon, 2019, **144**, 649–658.
[73] S. Chandrasekaran, C. Bowen, P. Zhang, Z. Li, Q. Yuan, X. Ren and L. Deng, Journal of Materials Chemistry A, 2018, **6**, 11078–11104.
[74] H. Dong, A. R. Oganov, Q. Zhu and G.-R. Qian, Scientific reports, 2015, **5**, 9870.
[75] M. Marqués, J. Osorio, R. Ahuja, M. Flórez and J. Recio, Physical Review B, 2004, **70**, 104114.
[76] E. Andrade, B. Costa, C. Chaves, A. de Paula, L. Cury, A. Malachias and G. Safar, Ultrasonics sonochemistry, 2018, **40**, 742–747.
[77] F. Mouhat and F. m. c.-X. Coudert, Phys. Rev. B, 2014, **90**, 224104.
[78] N. A. Zarkevich, H. Chen, V. I. Levitas and D. D. Johnson, Phys. Rev. Lett., 2018, **121**, 165701.
[79] X. Dong, A. R. Oganov, A. F. Goncharov, E. Stavrou, S. Lobanov, G. Saleh, G.-R. Qian, Q. Zhu, C. Gatti, V. L. Deringer, R. Dronskowski, X.-F. Zhou, V. B. Prakapenka, Z. Konpkov, I. A. Popov, A. I. Boldyrev and H.-T. Wang, Nature Chemistry, 2017, **9**, 440–445.
[80] H. Wu, X. Luo, L. Wen, H. Sun and C. Chen, Carbon, 2019, **144**, 161 – 170.
[81] G. K. Pradhan, A. Kumar, S. K. Deb, U. V. Waghmare and C. Narayana, Phys. Rev. B, 2010, **82**, 144112.
[82] M. Marqués, J. Osorio, R. Ahuja, M. Flórez and J. M. Recio, Phys. Rev. B, 2004, **70**, 104114.